A Numerical Algorithm for MHD of Free Surface Flows at Low Magnetic Reynolds Numbers

Roman Samulyak[1], Jian Du[2], James Glimm[1,2], Zhiliang Xu[1]
[1] *Computational Science Center,*
Brookhaven National Laboratory, Upton, NY 11973
[2] *Department of Applied Mathematics and Statistics,*
SUNY at Stony Brook, Stony Brook, NY 11794, USA

November 7, 2005

Abstract

We have developed a numerical algorithm and computational software for the study of magnetohydrodynamics (MHD) of free surface flows at low magnetic Reynolds numbers. The governing system of equations is a coupled hyperbolic/elliptic system in moving and geometrically complex domains. The numerical algorithm employs the method of front tracking for material interfaces, high resolution hyperbolic solvers, and the embedded boundary method for the elliptic problem in complex domains. The numerical algorithm has been implemented as an MHD extension of FronTier, a hydrodynamic code with free interface support. The code is applicable for numerical simulations of free surface conductive liquids or flows of weakly ionized plasmas. Numerical simulations of the Muon Collider/Neutrino Factory target have been discussed.

1 Introduction

Computational magnetohydrodynamics, greatly inspired over the last decades by the magnetic confinement fusion and astrophysics problems, has achieved significant results. However the major research effort has been in the area of highly ionized plasmas. Numerical methods and computational software for MHD of weakly conducting materials such as liquid metals or weakly ionized plasmas have not been developed to such an extent despite the need

for fusion research and industrial technologies. Liquid metal MHD, driven by potential applications of flowing liquid metals or electrically conducting liquid salts as coolant in magnetic confinement fusion reactors as well as some industrial problems, has attracted broad theoretical, computational, and experimental studies (see [16, 17, 18] and references therein). Weakly ionized plasmas have been studied with respect to their application to tokamak refueling devices [22, 23], laser ablation in magnetic fields [11], and other processes in a laboratory and nature.

The existance of free material interfaces in many practically important MHD porblems create major complications for numerical algorithms. The majority of numerical studies of free surface MHD flows is based on semi-analytical treatment of simplified flow regimes. The only fully numerical treatment of general free surface incompressible liquid flows is implemented in the HIMAG code [18] using the level set algorithm for fluid interfaces, electric potential formulation for electromagnetic forces, and incompressible fluid flow approximation. However, strong linear and nonlinear waves and other compressible fluid phenomena such as cavitation are typical features of many practically important free surface MHD regimes in both weakly ionized plasmas and liquid metals interacting with intense sources of external energies. The ablation of solid hydrogen pellets in tokamaks (a proposed tokamak fueling technology) [22, 23], laser - plasma interaction, and the interaction of liquid mercury jet with proton pulses in target devices for future advanced accelerators [20] are among numerous examples of such MHD problems. In this paper, we propose a 2D numerical algorithm and describe its implementation in a software package capable of studying such a class of problems. The work on the corresponding 3D version is in progress and will be reported in a forthcoming paper. The algorithm solves the compressible equations for fluid flows and the low magnetic Reynolds number approximation [19] for electromagnetic forces. Mathematically, the governing system of equations is a coupled hyperbolic - elliptic system in geometrically complex and evolving domains. We use the method of front tracking [8] for the propagation of fluid interfaces. Our FronTier code is capable of tracking and resolving of topological changes of large number of interfaces in two and three dimensional spaces [9]. In the method of front tracking, the interface is a Lagrangian mesh moving through a volume filling rectangular mesh according to the solution of the corresponding Riemann problem. High resolution solvers based on second order Godunov methods are used to update hyperbolic states in the interior away from interfaces. The embedded boundary method [14] is used for solving the elliptic problem in geometrically complex domains bounded by fluid interfaces. The explicit treatment

of interfaces typical for the method of front tracking is especially advantageous for multiphysics problems involving phase transitions. It allows not only to solve accurately the Riemann problem for the phase boundary [28], but also to apply different mathematical approximation in the regions separated by interfaces to account for the phase change from the solid to liquid and vapor phases as required, for instance, in the pellet ablation problems for the tokamak fueling.

In this paper, we also discuss results of the numerical simulation using the developed MHD code of the liquid mercury target for the Muon Collider/Neutrino Factory, a future advanced accelerator [20], http://www.cap.bnl.gov/mumu/info/intro.html. The target has been proposed as a liquid mercury jet interacting with an intense proton pulse in a 20 Tesla magnetic field. The state of the target after the interaction with a pulse of protons depositing a large amount of energy into mercury (the peak energy deposition is about 100 J/g) is of major importance to the accelerator design.

The paper is organized as follows. In Section 2, we introduce the system of governing equations and discuss mathematical approximations. The numerical algorithm and its implementation in the FronTier code and validation is described in Section 3. Applications of FronTier to the numerical simulation of the mercury target for the Muon Collider/Neutrino Factory is presented in Section 4. Finally, we conclude the paper with a summary of our results and perspectives for future work.

2 Governing Equations

The system of MHD equations [13, 19] contains a hyperbolic system of the mass, momentum and energy conservation equations for the fluid and a parabolic equation for the evolution of the magnetic field:

$$\frac{\partial \rho}{\partial t} = -\nabla \cdot (\rho \mathbf{u}), \tag{1}$$

$$\rho \left(\frac{\partial}{\partial t} + \mathbf{u} \cdot \nabla \right) \mathbf{u} = -\nabla P + \rho \mathbf{g} + \frac{1}{c} (\mathbf{J} \times \mathbf{B}), \tag{2}$$

$$\rho \left(\frac{\partial}{\partial t} + \mathbf{u} \cdot \nabla \right) e = -P \nabla \cdot \mathbf{u} + \rho \mathbf{u} \cdot \mathbf{g} + \frac{1}{\sigma} \mathbf{J}^2, \tag{3}$$

$$\frac{\partial \mathbf{B}}{\partial t} = \nabla \times (\mathbf{u} \times \mathbf{B}) - \nabla \times (\frac{c^2}{4\pi\sigma} \nabla \times \mathbf{B}), \tag{4}$$

$$\nabla \cdot \mathbf{B} = 0, \tag{5}$$

$$P = P(\rho, e). \tag{6}$$

Here $\mathbf{u}$, ρ and e are the velocity, density, and the specific internal energy of the fluid, respectively, P is the pressure, $\mathbf{g}$ is the gravitational acceleration, $\mathbf{B}$ is the magnetic field induction, $\mathbf{J} = \frac{c}{4\pi}\nabla \times \mathbf{H}$ is the current density distribution, and σ is the fluid conductivity. The magnetic field $\mathbf{H}$ and the magnetic induction $\mathbf{B}$ are related by the magnetic permeability coefficient μ: $\mathbf{B} = \mu\mathbf{H}$. In the system (1) - (4), we neglected effects of the heat conduction and viscosity. Equation (5) is the solenoidal property of the magnetic field, and (6) is the equation of state (EOS) that closes the system (1) - (4). We use the Gaussian units throughout the paper for all electromagnetic quantities except large values of the magnetic field which for convenience are given in Tesla.

The behavior of a fluid in the presence of electromagnetic fields is governed to a large extent by the magnitude of the conductivity. Being relatively poor conductors, most of liquid metals including mercury and weakly ionized gases are characterized by small diffusion times of the magnetic field

$$\tau = \frac{4\pi\mu\sigma L^2}{c^2},$$

where L is a characteristic length of the spatial variation of $\mathbf{B}$. If the eddy current induced magnetic field in such materials is also negligible compared to the external field, the system of equations (1) - (4) can be simplified using the low magnetic Reynolds number approximation [19]. If the magnetic Reynolds number

$$Re^M = \frac{4\pi v\sigma L}{c^2}$$

is small, the current density distribution can be obtained from Ohm's law

$$\mathbf{J} = \sigma\left(-\mathrm{grad}\phi + \frac{1}{c}\mathbf{u} \times \mathbf{B}\right), \tag{7}$$

where ϕ is the electric field potential. Due to the charge neutrality, the potential ϕ satisfies the following Poisson equation

$$\nabla \cdot (\sigma\nabla\phi) = \frac{1}{c}\nabla \cdot \sigma(\mathbf{u} \times \mathbf{B}). \tag{8}$$

For numerical computation, such an approach effectively removes fast time scales associated with the magnetic field diffusion. Equation (5) is automatically satisfied for an external magnetic field created by a realistic source.

The following boundary conditions must be satisfied at the interface Γ of a conducting fluid with a dielectric medium:

i) the normal component of the velocity field is continuous across the interface;

ii) the pressure jump at the interface is defined by the surface tension T and main radii of curvature:

$$\Delta P|_{\Gamma} = T\left(\frac{1}{r_1} + \frac{1}{r_2}\right); \tag{9}$$

iii) the normal component of the current density vanishes at the interface giving rise to the Neumann boundary condition for the electric potential

$$\left.\frac{\partial \phi}{\partial \mathbf{n}}\right|_{\Gamma} = \frac{1}{c}(\mathbf{u} \times \mathbf{B}) \cdot \mathbf{n}, \tag{10}$$

where $\mathbf{n}$ is a normal vector at the fluid free surface Γ.

In this paper, we propose a numerical algorithm for the MHD system of equations in low Re^M approximation (1) - (3), (7), (8) for free surface flows.

3 Numerical Algorithm and Implementation

The governing system of equations (1) - (3), (7), (8) is a coupled hyperbolic - elliptic system in a geometrically complex moving domain. The coupling of the hyperbolic and elliptic components is done using the operator splitting. The fluid interface is represented as an explicit co-dimension one Lagrangian mesh moving through a volume filling Eulerian mesh. The propagation and redistribution of the interface using the method of front tracking [2, 8] is performed at the beginning of the time step. Then interior states are updated by high resolution hyperbolic solvers such as the Monotonic Upstream-centered Scheme for Conservation Laws (MUSCL) [26]. At the end of the time step, the elliptic system is solved using the finite volume discretization with interface constraints in the spirit of the embedded boundary method [14], and the interior states are updated by adding electromagnetic source terms. In the next two sections, we describe numerical algorithms for the hyperbolic and elliptic subsystems and their implementation in the FronTier code.

3.1 Hyperbolic problem and free surface propagation

Front tracking is an adaptive computational method in which a lower dimensional moving grid is fit to and follows distinguished waves in a flow.

Tracked waves explicitly include jumps in the flow state across the waves and keep discontinuities sharp. A key feature is the avoidance of finite differencing across discontinuity fronts and thus the elimination of interfacial numerical diffusion including mass and vorticity diffusion [2, 8]. Front tracking is implemented in FronTier [9, 10], a multiphysics code which is capable of tracking and resolving topological changes of geometrically complex interfaces in two and three space dimensions. Details of the front tracking method and the structure of the FronTier code are described in the above mentioned papers. In this section, we will describe only details of the algorithm specific to the MHD system.

For free surface MHD flows, we are interested in tracking only fluid interfaces which are contact discontinuity curves of the corresponding Riemann problem [5]. The interface propagation consist of normal and tangential propagation of each interface point. Since the tangential propagation in the MHD case is essentially equivalent to the algorithm described in [10], we will concentrate here only on the algorithm for the normal propagation of interface points.

In the operator splitting scheme, the system of equations (1) - (3) can be considered as a pure hydrodynamic system in an external field given by the Lorentz force. Since this force depends on material properties, the interface propagation algorithm is different from that for the gravity force [10]. Normal point propagate seeks to solve a generalized Riemann problem for the projection of the flow equations onto the direction normal to the front at the point being propagated. The projection of the system (1) - (3) into the normal direction $\mathbf{N}$ yields the following one dimensional system

$$
\begin{aligned}
&\frac{\partial \rho}{\partial t} + \frac{\partial \rho v_N}{\partial \mathbf{N}} + \frac{\alpha N_0}{r}\rho v_N = 0,\\
&\frac{\partial \rho v_N}{\partial t} + \frac{\partial \left(\rho v_N^2 + P\right)}{\partial \mathbf{N}} + \frac{\alpha N_0}{r}\rho v_N^2 = \rho g_N + \frac{1}{c}(\mathbf{J}\times\mathbf{B})_N,\\
&\frac{\partial \rho v_T}{\partial t} + \frac{\partial \rho v_N \mathbf{v}_T}{\partial \mathbf{N}} + \frac{\alpha N_0}{r}\rho v_N \mathbf{v}_T = 0,\\
&\frac{\partial \rho E}{\partial t} + \frac{\partial \left(\rho E v_N + P v_N\right)}{\partial \mathbf{N}} + \frac{\alpha N_0}{r}\left(\rho E v_N + P v_N\right) = \rho g_N v_N.
\end{aligned}
\tag{11}
$$

Here N_0 is the r component of the normal vector $\mathbf{N}$, $\partial/\partial\mathbf{N} = \mathbf{N}\cdot\nabla$ is the directional derivative in the direction $\mathbf{N}$, $A_\mathbf{N} = \mathbf{A}\cdot\mathbf{N}$ is the normal component of a vector field $\mathbf{A}$ and $A_T = \mathbf{A} - A_\mathbf{N}\mathbf{N}$ is the corresponding tangential component. The parameter α is equal to 1 for cylindrical coordinate system axially symmetric with respect to z axis, 2 for spherical coordinate system,

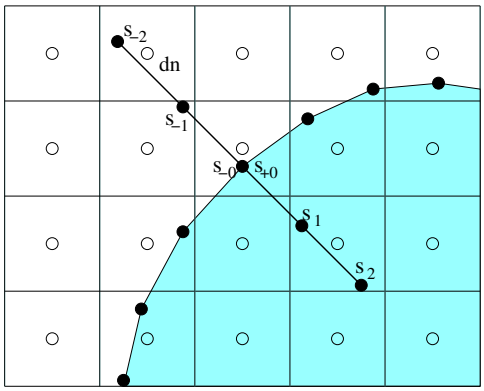

Figure 1: Schematic of a stencil for the normal point propagation algorithm.

and 0 otherwise. The implementation of geometric source terms corresponding to the cylindrical and spherical systems of coordinates is given in [10].

A 5-point stencil for the point propagation algorithm is schematically shown in Figure 1. The algorithm has three main steps: slope reconstruction to compute approximation to the flow gradients along the normal line, prediction using the Riemann problem solution, and correction to account for the flow gradients on both sides of the front and to include geometric and body terms.

The reconstructions step is standard and used in many shock capturing methods. In the prediction step (see Figure 2a), we solve the Riemann problem with states s_{-0} and s_{+0} to calculate the interface velocity W_0 at the beginning of the time step. Using this velocity, we can estimate the position of the interface x_I at the end of the time step. The middle states of the solution of the Riemann problem also provide the interface states s_{-I} and s_{+I} at the new interface position x_I. The correction step starts with obtaining states connected by characteristics with the states at the predicted interface position. Namely, we trace back the incoming characteristics from the predicted new front position using the velocity and sound speeds computed from the Riemann problem, and use the slope reconstruction algorithm to approximate the states sf and sb at the feet of characteristics (Figure 2b). Then the Riemann problem with the input states s_f and s_{-0} is solved and the right wave state of the solution, s_{ll}, approximates the wave incoming on the contact at time $t_0 + dt$ from the left. Correspondingly, the Riemann problem with the input states s_b and s_{+0} is solved and the left wave state of the solution, s_{rr}, approximates the wave incoming on the contact at time $t_0 + dt$ from the right. The states s_{ll}, and s_{rr} are then modified by the action

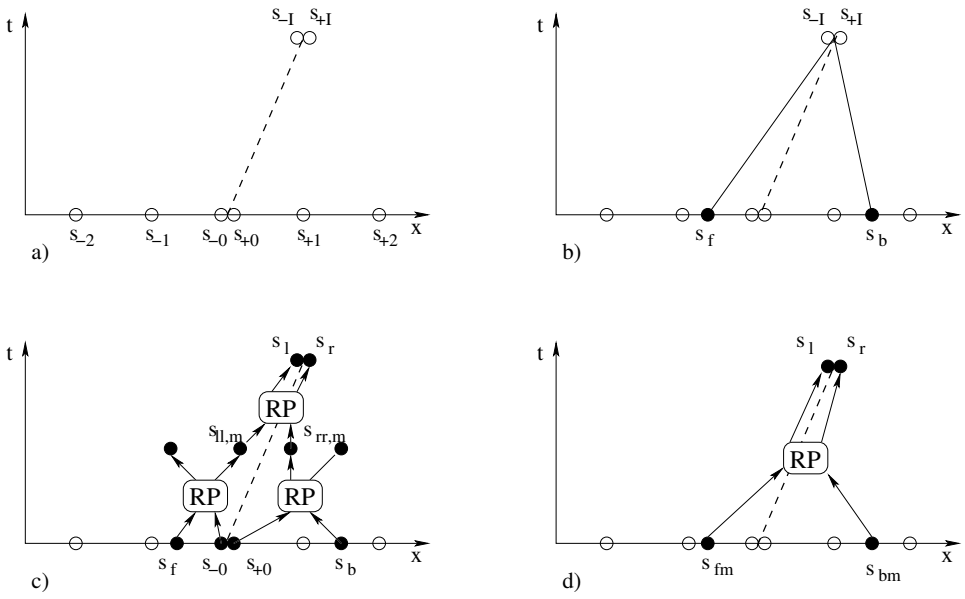

Figure 2: Schematic of a the normal point propagation algorithm. RP denotes the procedure of solving the Riemann problem and extracting of the middle states from the solution.

of the Lorentz force which was computed at the previous time step. The resulting states s_{llm}, and s_{rrm} approximate the state of the flow at the end of the time step. Notice that in most of practical calculations only the left or right pair of states has to be modified since the conducting fluid is on only one side of the interface. Finally, the Riemann problem with the input state s_{llm} and s_{rrm} is solved to obtain approximations of the left and right states at the front, s_l and s_r, and the front velocity V at the time $t_0 + dt$. The procedure is illustrated in Figure 2c. Assuming that the acceleration of the interface is constant during the time step, the interface velocity *during the time step* is approximated as $W = (W_0 + V)/2$. However if strong waves are not present in the vicinity of the interface, we simplify the algorithm and approximate the final interface states by solving the Riemann problem with the input states s_{fm} and s_{bm} obtained from states s_f and s_b by the action of the Lorentz force as shown in Figure 2d. This allows to reduce the computational time by eliminating two relative expensive Riemann problem steps for every interface point.

Two techniques for the redistribution of interfaces and resolving their topological changes, the grid free and grid based tracking, have been devel-

oped [9]. In the first method, interface points are always independent of the rectangular grid while in the second method the interface points are formed by the intersection of the interface with the rectangular grid lines. Since the first algorithm is more accurate and sufficiently robust, especially in 2D, we use it for the interface propagation in the hyperbolic part of the MHD algorithm. However we always transform the interface to the grid based one at the beginning of the elliptic time step since such an interface ideally suits our finite volume discretization technique for the Poisson equation described in the next section. Notice that in many practical applications, it is sufficient to perform the expensive elliptic step once per several hyperbolic time steps.

The final phase of the hyperbolic time step update consists of computing new states on the rectangular spatial grid. Several different shock capturing methods have been implemented in FronTier. They include both directionally splitted MUSCL (Monotonic Upstream-centered Scheme for Conservation Laws [26]) type schemes such as the Piecewise Linear, Piecewise Parabolic Method [3], a second order MUSCL scheme developed by I. L. Chern, and an unsplit MUSCL scheme [4]. Several exact and approximate Riemann solvers are available for use by these methods.

3.2 Elliptic problem for irregular domains

The embedded boundary method is based on the finite volume discretization in grid cells. The domain boundary is embedded in the rectangular Cartesian grid, and the solution is treated as a cell-centered quantity, even when these centers are outside of the domain. This treatment has the advantages of dealing with geometrically complex domains and ensures second-order accuracy of solutions [14].

We will describe the method and implementation for the MHD elliptic problem, namely the Poisson equation (8) with Neumann boundary condition (10). Using the divergence theorem and integrating the flux $\mathbf{f} = \sigma\nabla\varphi$ over the control volume, the differential operator can be discretized as

$$(L\varphi)_{\Delta_{i,j}} = \frac{1}{area_{i,j}}\Big(\sum_k F_k l_k + F^f l_f\Big) \tag{12}$$

where $area_{i,j}$ is the area of the control volume,F_k is evaluated at the middle point of all cell edges, and l_k is the corresponding edge length. For full cell edges (not cut by the boundary),F_k is obtained by centered difference while for partial cell edges it is the linear interpolation between values at the midpoints of full edges. The flux F^f across the domain boundary, as in

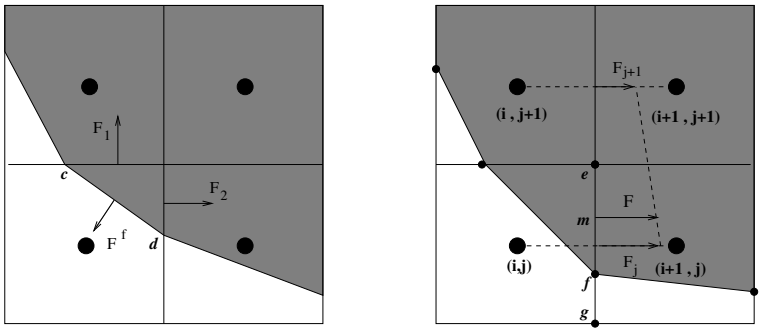

Figure 3: Linear interpolation of flux

the left part of Fig. 3, is given by the Neumann boundary condition and l_f equals the length of the boundary edge cd. The linear interpolation for the partial cell edge flux F is shown on the right with

$$F_{j+1} = \frac{\varphi_{i+1,j+1} - \varphi_{i,j+1}}{h_x} \; ; \; F_j = \frac{\varphi_{i+1,j} - \varphi_{i,j}}{h_x}$$

$$F = \sigma_m \Big(\frac{(1+a)}{2} F_j + \frac{(1-a)}{2} F_{j+1} \Big)$$

where $a = \frac{|ef|}{|eg|}$ is length fraction of the partial cell edge,h_x is the grid spacing in x direction and σ_m is evaluated at m, the middle point of the edge ef.

In order to implement the embedded boundary method, the interface is reconstructed using its intersections with grid lines. The following assumptions and simplifications are made. The number of intersection of each grid cell with the boundary curve must be either 0 or 2. This is generally satisfied when curvature of interface is not too large or the grid is fine enough. As a result, there are only three possible configurations for the partial cells cut by the boundaries, triangle, trapezoid and pentagon, as shown in Fig 4. The other approximation is that the positions of the boundary points are adjusted to remove cells with volumes less than certain preset value. This means to shift the points mostly by a distance of tolerance$\cdot h$,where h is the grid spacing. This modification is necessary since cells of arbitrary small volumes introduce large numerical errors and increase the condition number for the discretized linear system.

We summarize our implementation of the algorithm as follows:
(1) The elliptic domain boundary is constructed using intersection points

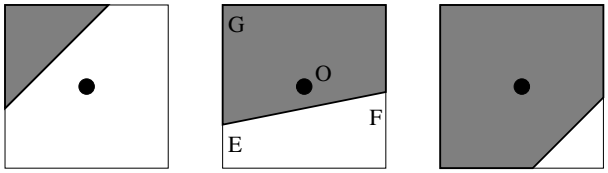

Figure 4: Possible configurations of partial cell

of the grid free interface with grid lines. With the information from the reconstruction, material components type of both the grid points and cell centers are also properly set.

(2) All grid cells are divided into three types: FULL, PARTIAL and EXTERNAL, which mean completely within, partially within, and completely outside of the computational domain for the elliptic problem. During the procedure of counting blocks, both FULL and PARTIAL cell are counted and the total number is gathered from all processors and used to set the matrix dimension for the linear system.

(3) Local and global coordinates of finite volume cells are stored, and the buffer zone is created for subdomains via MPI communication between neighboring processors. This is needed for two reasons. One is for the finite volume discretization, the other is to calculate the flux across the subdomain boundaries after solving the linear system.

(4) With the relative positions of crossings and material components at grid corners, the configuration of partial cells can be uniquely determined. Then stencils for the discrete Laplacian operator are chosen and the corresponding coefficients are inserted into the matrix. The stencil choice for a pentagon partial cell is illustrated in Fig. 5. a and b, as in Figure 3 correspond to the length fractions of the related edges. The finite volume discretization can be written as:

$$(L\varphi)_{\Delta_{i,j}} = \sum_{p=i-1}^{i+1} \sum_{q=j-1}^{j+1} c(p,q)\varphi_{p,q} + F^f l_f$$

$$c(i,j) = \frac{1}{area}\Big(- \sigma_2 \frac{hx}{hy} - \sigma_3 \frac{hy}{hx} - \sigma_4 \frac{b(1+b)hx}{2hy} - \sigma_1 \frac{a(1+a)hy}{2hx}\Big)$$

$$c(i,j-1) = \frac{1}{area}\Big(\sigma_4 \frac{b(1+b)hx}{2hy}\Big);\ c(i-1,j) = \frac{1}{area}\Big(\sigma_1 \frac{a(1+a)hy}{2hx}\Big)$$

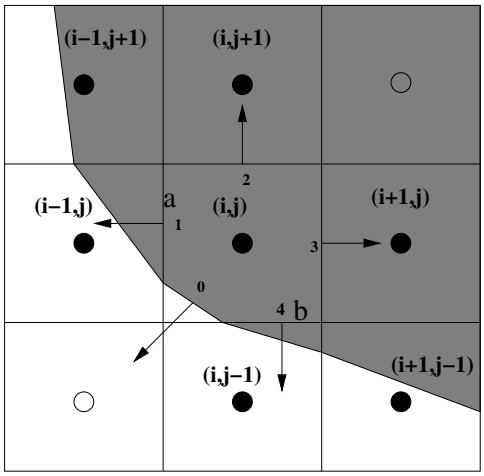

Figure 5: Stencil setting for partial cell

$$c(i+1,j-1)=\frac{1}{area}\Big(\sigma_4\frac{b(1-b)hx}{2hy}\Big);\ c(i-1,j+1)=\frac{1}{area}\Big(\sigma_1\frac{a(1-a)hy}{2hx}\Big)$$

$$c(i,j+1)=\frac{1}{area}\Big(\sigma_2\frac{hx}{hy}-\sigma_1\frac{a(1-a)hy}{2hx}\Big);\ c(i+1,j)=\frac{1}{area}\Big(\sigma_3\frac{hy}{hx}-\sigma_4\frac{b(1-b)hx}{2hy}\Big)$$

$$c(i-1,j-1)=c(i+1,j+1)=0$$

σ_i(i = 1,2,3,4) are evaluated at cell edge centers(points 1,2,3 and 4 in Fig. 5) and term F^f and l_f with the same meaning as in equation (12).

(5) The boundary flux in equation (10), determined explicitly by the Neumann Boundary conditions, is moved to the right side. Since the right hand side, which must be evaluated at the centroid of a partial cell, has the divergence form of a vector field ($\nabla\cdot(\mathbf{u}\times\mathbf{B})$), the divergence theorem is applied to replace the divergence with finite volume integration of flux across boundary. This cancels the gradient of potential and flux of $\mathbf{u}\times\mathbf{B}$ in the normal direction to the boundary since they are equal by the boundary condition.

(6) The resulting linear system is solved. We use preconditioners and iterative solvers implemented in PETSc [1] and HYPRE [12] libraries.

(7) The gradient of the potential is calculated via finite differences and the current density is calculated from equation (7). Then the interior momentum states are modified by adding the Lorentz force term. Notice that if the hyperbolic system is written in terms of conserved variables, namely

the density, momentum, and total energy density, the last variable remains unchanged. It is easy to verify that the external magnetic field does not change the total energy of the system, and the increase of the internal energy due to Joule's heat is canceled by the decrease of the kinetic energy due to the Lorentz force.

3.3 Validation of the elliptic technique

An extensive theoretical analysis of the method of front tracking for hyperbolic systems of conservations laws has already been done, and the method has been validated and tested on problems of Rayleigh-Taylor and Richtmyer-Meshkov surface instabilities (see for example [6, 7] for the comparison of theoretical, numerical, and experimental data of Rayleigh-Taylor mixing rates). Since the described elliptic technique is new to the method of front tracking and the FronTier software, we have validated it using analytical solution of a simple elliptic problem. Namely, we solve numerically the Neumann problem

$$\begin{aligned} \varphi_{xx} + \varphi_{yy} &= \mathbf{f}, \\ \left.\frac{\partial \varphi}{\partial \mathbf{n}}\right|_{\Gamma} &= g, \end{aligned}$$

with $\mathbf{f}$ and g obtained by differentiating the exact solution $\varphi = e^{k_1 x^2 + k_2 y^2}$. The problem is solved in an irregular domain shown in Figure 6.

Since the Neumann boundary problem has solution with an arbitrary constant, we only show the convergence behavior of the gradient of the solution. The convergence rate R is given by the formula:

$$R = \log\left(\frac{\| e_{n+1} \|}{\| e_n \|}\right) \Big/ \log\left(\frac{h_{n+1}}{h_n}\right)$$

e_{n+1} and e_n are error vectors corresponding to grid spacing h_{n+1} and h_n. In our calculation, the 2-dimensional $l_{2,\Delta x}$ norm is used. From Table 1, we can conclude that the computed gradient of solution has the first order accuracy, therefore the computed potential is second order accurate. In Fig. 7, the contour of the gradient error in the x direction is shown for grid 64x64 (left) and grid 128x128 (right). With the setting of a Dirichlet point and eliminating the constant from the solution, we can also conclude that the accuracy of the computed solution is of second order. All test calculations were performed on 4 processors using a 2x2 domain decomposition.

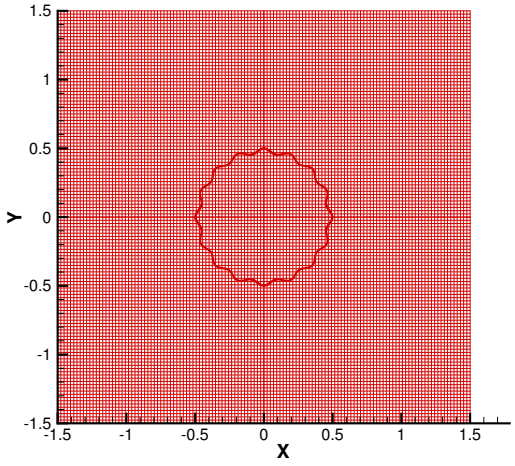

Figure 6: Computational domain

Table 1: Convergence results for the gradient of the solution

mesh size	error φ_x	R
32x32	2.4961e-02	N/A
64x64	8.8409e-03	1.497
128x128	3.0935e-03	1.506
256x256	1.0957e-03	1.503

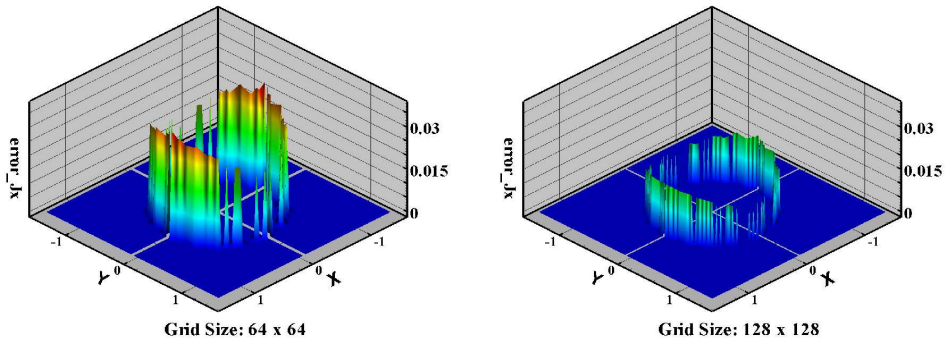

(a) (b)

Figure 7: Error of the calculated gradient of the potential in x direction

4 Application: Numerical Simulation of the Muon Collider/Neutrino Factory Target Experiment.

In this section, we present results of the numerical simulation of a liquid mercury jet interacting with an intensive proton pulse in a 20 Tesla magnetic field. Such a jet will be used as a target in the proposed Muon Collider/Neutrino Factory [20]. The target is shown schematically in Figure 8. It will contain a series of mercury jet pulses of about 0.5 cm in radius and 60 cm in length. Each pulse will be shot at a velocity of 30-35 m/sec into a 20 Tesla magnetic field at a small angle (0.1 rad) to the axis of the field. When the jet reaches the center of the magnet, it is hit with a 3 ns proton pulse depositing about 100 J/g of energy in the mercury.

The actual energy deposition in the mercury jet due to the interaction with protons was calculated using a Monte-Carlo code MARS [20]. The energy deposition profile can be accurately approximated by a two-dimensional Gaussian function in cylindrical coordinates. Since the angle between the jet axis and the magnetic field lines is small, the off-axial component of the magnetic field can be ignored for the study of short time scale hydrodynamic processes caused by the proton energy deposition (the off-axial magnetic field could not be ignored in the study of some other aspects of this problem, for example the relatively long time scale entrance of the jet

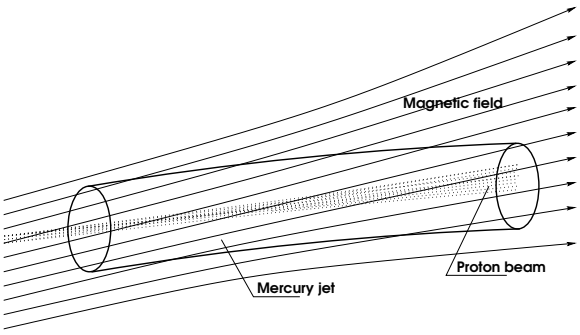

Figure 8: Schematic of the target for the Muon Collider/Neutrino Factory.

into the magnetic field). In the assumption of a uniform magnetic field, only the radial motion of the mercury induces eddy currents. We have performed 2d numerical simulations in the transverse plane intersecting the jet at the maximum point of energy deposition. Other hydro and MHD aspects of the target problem were studied numerically in [24, 25].

The influence of the 3 ns proton pulse was modeled by adding the proton beam energy density to the internal energy density of mercury at a single time step which caused the increase of pressure to 16 kbar in the center. Strong pressure waves in the mercury jet cause the jet expansion. Previous numerical simulations performed with a single phase equation of state (EOS) for liquid mercury (stiffened polytropic EOS) have shown that the strength of rarefaction waves in the jet significantly exceeds the mercury cavitation threshold. We believe that the formation of cavities takes place in strong rarefaction waves, and cavitation bubbles influence the wave dynamics in mercury and the jet surface evolution. This conclusion is supported by first targetry experiments on the jet - proton pulse interaction without the magnetic field [15]. In order to capture the formation and dynamics of the two-phase domain of bubbly mercury, we have used a simple homogenized two-phase equation of state [25]. The EOS consists of three branches. The pure vapor and liquid branches are described by the polytropic and stiffened polytropic [21] EOS models, respectively, reduced to a single isentrope. The two branches are connected by a model for the liquid-vapor mixture

$$P = P_{sat,l} + P_{vl}\log\left[\frac{\rho_{sat,v}{a_{sat,v}}^2(\rho_{sat,l} + \alpha(\rho_{sat,v} - \rho_{sat,l}))}{\rho_{sat,l}(\rho_{sat,v}{a_{sat,v}}^2 - \alpha(\rho_{sat,v}{a_{sat,v}}^2 - \rho_{sat,l}{a_{sat,l}}^2))}\right],$$

where $\rho_{sat,v}$, $\rho_{sat,l}$, $a_{sat,v}$, $a_{sat,l}$ are the density and the speed of sound of vapor and liquid in saturation points, respectively, $P_{sat,l}$ is the liquid pressure

in the saturation point, α is the void fraction

$$\alpha = \frac{\rho - \rho_{sat,l}}{\rho_{sat,v} - \rho_{sat,l}},$$

and the parameter P_{vl} is

$$P_{vl} = \frac{\rho_{sat,v} {a_{sat,v}}^2 \rho_{sat,l} {a_{sat,l}}^2 (\rho_{sat,v} - \rho_{sat,l})}{\rho_{sat,v}{}^2 {a_{sat,v}}^2 - \rho_{sat,l}{}^2 {a_{sat,l}}^2}.$$

These expressions were derived by integrating an experimentally validated model for the sound speed in a bubbly mixture [27]. The conductivity of the two-phase mixture of mercury was approximated as a linear function of the void fraction

$$\sigma(\mathbf{x}, t) = (1 - \alpha(\mathbf{x}, t))\sigma_0,$$

where $\sigma_0 = 10^{16} s^{-1}$ is the conductivity of liquid mercury at normal conditions.

Our simulations show that pressure waves in the mercury jet caused by the proton energy deposition lead to the formation of a two-phase cavitation domain in the center and the jet (see Figures 9(a) and 11). However the jet cavitation and expansion are strongly reduced in a magnetic field and almost completely suppressed when the magnetic field strength reaches 20 Tesla (see Figures 9(d) and 11(b)). These results are in agreement with numerical simulations performed earlier using simple approximations [25]. Figure 10 shows schematically the distribution of the electric current density in the jet induced by the radial expansion. It is easy to see that the corresponding Lorentz force reduces the jet expansion. The jet expansion velocity at $B = 0$ calculated from the graph 11(a) is in a very good agreement with experimentally measured values [15], which give us a confidence in predictive capabilities of the equation of state for the two phase mixture and EOS parameters. All past experiments have been performed without magnetic fields but the preparation for a new series of experiments involving mercury jets interacting with powerful proton beams and in a 15 Tesla solenoid are underway at CERN, Geneva.

Notice that although small amplitude perturbations were imposed initially on the jet surface, the late time jet evolution did not exhibit surface instabilities (see Figure 9). This surface smoothening was caused by the use of the homogenized equation of state for cavitating fluid. Due to averaging of fluid properties on relatively large spatial scales, such an EOS makes it impossible to study complex wave patterns at small scales that influence surface perturbations. To improve the cavitation modeling and simulation

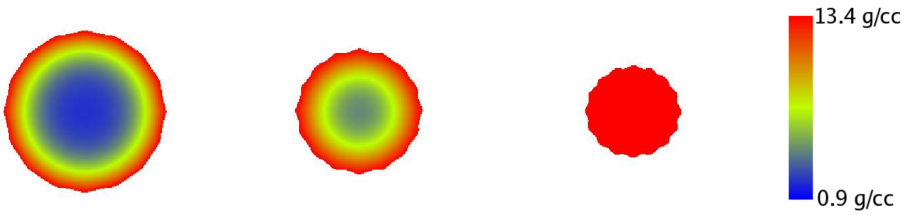

(a) B = 0 (b) B = 10 Tesla (c) B = 20 Tesla (d)

Figure 9: Density distribution in the cross-section of the mercury jet at $t = 160$ microseconds in magnetic fields ranging from 0 to 20 Tesla

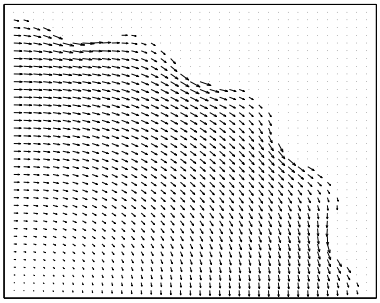

Figure 10: Distribution of the induced current density in the jet cross-section

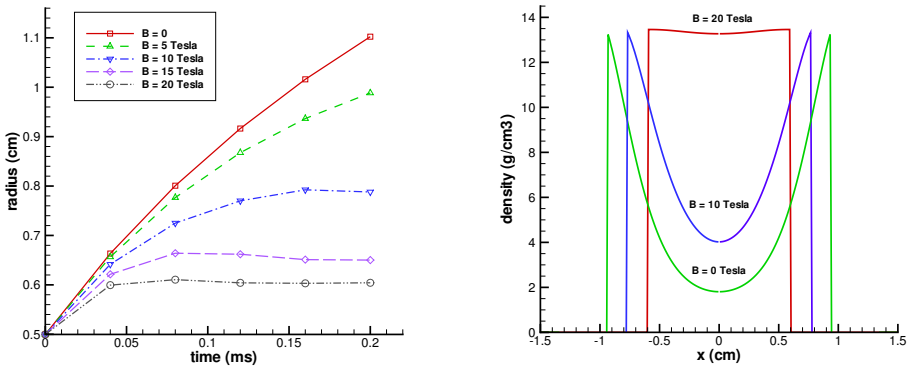

(a) Evolution of the mercury jet radius.

(b) Density profile in the jet cross-section at $t = 130$ microseconds

Figure 11: Mercury jet evolution in magnetic fields ranging from 0 to 20 Tesla

of wave dynamics in the presence of cavitation bubbles at small scales, we have developed a numerical algorithm for the dynamic creation of explicitly tracked cavitation bubbles [28]. Results of the direct numerical simulation in the mercury jet in the presence of a magnetic field will be presented in a forthcoming paper.

5 Conclusions

We have developed a numerical algorithm and computational software for the numerical simulation of fundamental and applied problems of free surface magnetohydrodynamic (MHD) flows at low magnetic Reynolds numbers of compressible conducting liquids partially ionized plasmas in the presence of phase transitions and high power particle and laser beams. The corresponding governing equations constitute a coupled hyperbolic - elliptic system in geometrically complex and evolving domains. The numerical algorithm includes the interface tracking technique for hyperbolic problems, modified Riemann solvers for phase boundaries, meshing and discretization of elliptic equations in complex domains with interface constraints using the embedded boundary method, and high performance parallel solvers such as MUSCLE-type schemes for hyperbolic problems and iterative solvers implemented in

the PETSc and HYPRE packages. An extensive theoretical analysis of the method of front tracking for hyperbolic systems of conservations laws has already been done, and the method has been validated and tested on problems of Rayleigh-Taylor and Richtmyer-Meshkov surface instabilities. The elliptic algorithm is second order accurate for the electric potential except for the interface. It, however, does not significantly reduce the accuracy of the method since the electromagnetic forces on the interface, as it was shown in Section 3.1, are obtained by propagating states along characteristics from interior to the interface in most of practical cases. The method was validated in the current work using analytical solutions of a simple elliptic problem.

The MHD algorithm has been applied for the numerical simulations of liquid mercury target for the Muon Collider/Neutrino Factory. The target has been proposed a mercury jet interacting with an intense proton pulse in a 20 Tesla magnetic field. Our simulation used a homogenized EOS for two-phase liquid in order to capture the rarefaction wave induced cavitation in the mercury jet and the jet expansion. The numerically computed velocity of the jet expansion agrees quantitatively with experimental data. We showed that the magnetic field reduces both the jet cavitation and expansion. These results are in qualitative agreement with previous simulations which used other simplifying assumptions.

Other current and future applications of developed models and software include such challenging projects as refueling of tokamaks through the injection of frozen deuterium pellets, and the laser driven acceleration of pellets by ablation recoil (rocket) effect. Applied research is being done in collaboration with General Atomics Fusion Group, Muon Collider/Neutrino Factory Collaboration, and Princeton Plasma Physics Laboratory.

Acknowledgments: We thank members of the Muon Collider/Neutrino Factory Collaboration for useful discussions and for partial support of work presented here.

References

[1] S. Balay, W. Gropp, L. McInnes and B. Smith, PETSc Users Manual, ANL-95/11 - Revision 2.1.1, Argonne National Laboratory, 2001.

[2] I. R. Chern, J. Glimm, O. McBryan, B. Plohr, S. Yaniv, Front tracking for Gas Dynamics, J. Comput. Phys. 62 (1986) 83-110.

[3] P. Colella, P. Woodward, The piesewise parabolic method (PPM) for gas-dynamical simulations, J. Comput. Phys. 54 (1984) 174.

[4] P. Colella, Multidimensional upwind methods for hyperbolic conservation laws, J. Comput. Phys. 87 (1990) 171-200.

[5] R. Courant, K. Friedrichs, Supersonic Flows and Shock Waves, Interscience, New York, 1948.

[6] E. George, J. Glimm, Self similarity of Rayleigh-Taylor mixing rates, Phys. Fluids 17 (2005).

[7] E. George, J. Glimm, X. L. Li, A. Marchese, Z. L. Xu, A Comparison of Experimental, Theoretical, and Numerical Simulation Rayleigh-Taylor Mixing Rates, Proc. National Academy of Sci. 99 (2002) 2587-2592.

[8] J. Glimm, J. Grove, X. L. Li, K. L. Shyue, Q. Zhang., Y. Zeng, Three dimensional front tracking, SIAM J. Sci. Comp. 19 (1998) 703-727.

[9] J. Glimm, J. Grove, X. L. Li, D. C. Tan, Robust computational algorithms for dynamic interface tracking in three dimensions, SIAM J. Sci. Comp. 21 (2000) 2240-2256.

[10] J. Glimm, J. Grove, Y. Zhang, Interface tracking for axisymmetric flows, SIAM J. Sci. Comp. 24 (2002) 208-236.

[11] S. S. Harilal, M. S. Tillack, B. O Shay, C. V. Bindhu, F. Najmabadi, Confinement and dynamics of laser produced plasma expanding across a transverse magnetic field, UCSD-ENG-106, 2003.

[12] Hypre: high performance preconditioners: user's manual, http://www.llnl.gov/CASC/hypre/software.html

[13] D. J. Jackson, Classical Electrodynamics, John Wiley & Sons, New York-Toronto-Singapore, 1974.

[14] H. Johansen, P. Colella, A Cartesian grid embedded boundary method for Poisson's equation on irregular domains, J. Comput. Phys. 147 (1998) 60-85.

[15] H. Kirk, et al., Target studies with BNL E951 at the AGS, Particles and Accelerators 2001, Chicago IL, June 18-22 2001.

[16] S. Molokov, C. B. Reed, Review of free-surface MHD experiments and modeling, Technical Report ANL/TD/TM99-08, Argonne National Laboratory, 1999.

[17] N. Morley, S. Smolentsev, L. Barleon, and I. Kirillov, Liquid magnetohydrodynamics - recent progress and future directions for fusion, Fusion Engineering and design (2000) 51-52, 701-713.

[18] N. Morley, S. Smolentsev, R. Munipalli, M.-J. Ni, D. Gao, M. Abdou, Progress on the modeling of liquid metal, free surface MHD flows for fusion liquid walls, Fusion Engineering and Design 72 (2004) 3-34.

[19] R. Moreau, Magnetohydrodynamics, Kluwer Academic Publishers, Dordrecht-Boston-London, 1990.

[20] Ozaki, S., Palmer, R., Zisman, M., Gallardo, J. (editors): Feasibility Study- II of a Muon-Based Neutrino Source, BNL-52623 (2001).

[21] R. Menikoff, B. Plohr, The Riemann problem for fluid flow of real materials, Rev. Mod. Phys. 61 (1989) 75-130.

[22] P. Parks, R. Turnbull, Effect of transonic flow in the ablation cloud on the lifetime of a solid hydrogen pellet in plasma, Phys. Fluids 21 (1978) 1735-1741.

[23] P. Parks, Magnetic-field distortion near an ablating hydrogen pellet, Nuclear Fusion 20 (1980) 311-320.

[24] R. Samulyak, Numerical simulation of hydro- and magnetohydrodynamic processes in the Muon Collider target, Lecture Notes in Comp. Sci. 2331 (2002) 391-400, Springer-Verlag, Berlin-Heidelberg, 2002.

[25] R. Samulyak, Y. Prykarpatskyy, Richtmyer-Meshkov instability in liquid metal flows: influence of cavitation and magnetic fields, Mathematics and Computers in Simulations 65 (2004) 431-446.

[26] B. van Leer, Towards the ultimate conservative difference scheme: V. A second order sequel to Godunov's method, J. Comput. Phys. 32 (1979) 101-136.

[27] Wijngaarden, L. Van: One-dimensional flow of liquids containing small gas bubbles. Ann. Rev. Fluid Mech. 4 (1972) 369-396.

[28] Z. Xu, M.N. Kim, W. Oh, J. Glimm, R. Samulyak, X.L. Li, and C. Tzanos, Atomization of a High Speed Jet, Phys. Fluids, 2005, Submitted.